ELECTRONIC RESEARCH ARCHIVE
Volume **28**, Number **2**, June **2020**

doi:10.3934/era.2020062
pp. **1123–1142**

# A NEURAL NETWORK METHOD FOR THE INVERSE SCATTERING PROBLEM OF IMPENETRABLE CAVITIES

Weishi Yin[1,2,*]

[1] Experiment Centre of Mathematics, Changchun University of Science and Technology
Changchun 130022, China

Jiawei Ge[2], Pinchao Meng[1,2] and Fuheng Qu[3]

[2] College of Science, Changchun University of Science and Technology
Changchun 130022, China

[3] School of Computer Science and Technology, Changchun University
of Science and Technology, Changchun 130022, China

Abstract. This paper proposes a near-field shape neural network (NSNN) to determine the shape of a sound-soft cavity based on a single source and several measurements placed on a curve inside the cavity. The NSNN employs the near-field measurements as input, and the output is the shape parameters of the cavity. The self-attention mechanism is employed to obtain the feature information of the near-field data, as well as the correlations among them. The weights and biases of the NSNN are updated through the gradient descent algorithm, which minimizes the error of the reconstructed shape of the cavity. We prove that the loss function sequence related to the weights is a monotonically bounded non-negative sequence, which indicates the convergence of the NSNN. Numerical experiments show that the shape of the cavity can be effectively reconstructed with the NSNN.

1. **Introduction.** The exterior scattering problem is a typical inverse scattering problem, where scattering objects are illuminated by incident waves from the exterior of the objects, and the measurements are also taken outside [8]. Examples of this problem appear in a wide range of applications, such as geophysical explorations, sonar and radar techniques, etc. However, in some practical applications, it is necessary to use non-destructive testing to detect the structural integrity of the cavity. In some industrial applications, the transmitters and receivers are placed in the cavity, structural integrity of which is then tested through source (incident waves) and measurements (scattering waves) [12]. In this case, the inverse scattering problem is called interior inverse scattering problem. In this paper, we investigate the approach to recover the shape of the cavity by using the near-field data. This study is based on the Dirichlet boundary condition and the near-field data produced by the cavity and the single point source.

In recent years, the interior inverse scattering problems of cavity have attracted widespread attention, and some classical numerical methods have been proposed

2020 *Mathematics Subject Classification.* 65.

*Key words and phrases.* Inverse scattering problem, near-field data, cavity, artificial neural network, convergence.

The research of first author is supported by National Natural Science Foundation of China grant 11671107.

* Corresponding author: Weishi Yin.

to the solution. In [22], Qin and Cakoni employed a Newton-type optimization technique for an equivalent nonlinear integral equation to solve the inverse interior scattering problem for an impenetrable cavity with the Dirichlet boundary condition. Qin and Colton [23] proved the uniqueness of the inverse scattering problem of impenetrable cavity with the Dirichlet boundary condition. In their study, the shape and position of the cavity were retrieved by the linear sampling method (LSM). They further extended their method to reconstruct both the shape of the cavity and the surface impedance of the cavity in literature [24]. Cakoni et al. [6] established a LSM to determining the shape of a penetrable cavity, and proved the uniqueness through an unusual non-selfadjoint eigenvalue problem. Hu et al. [11] used the LSM to determine both the shape and boundary impedance of the partially coated cavity. In addition to the LSM, Zeng et al. [32] employed the decomposition method to reconstruct the cavity and present some convergence results. Liu [16] used the factorization method (FM) to solve inverse scattering problem of the cavity. In [15], the near-field imaging method is developed to solving the inverse problem of reconstructing the shape of an interior cavity. Sun et al. [28] applied the reciprocity gap (RG) functional method and determine the shape of the cavity from the Cauchy data on a curve inside the cavity, they also indicated the equivalence of the RG functional method and the LSM with mere the scattered field. Karageorghis et al. [13] employed the method of fundamental solutions (MFS) to detect a sound-soft scatterer surrounding host acoustic homogeneous medium due to a given point source inside it. Recently, Zhang et al. [33] proposed the idea of using a reference ball and the superimposition of two point sources as incident waves, and proved that the position, shape and boundary conditions of the cavity can be uniquely determined from phaseless near-field data. More studies on the inverse scattering problems of the cavities can also be found in [2, 10, 25].

The interior scattering problem is physically more complicated than the usual exterior scattering problem in some aspects. In the former situation, all of the scattered waves are "trapped", i.e., the scattered waves are reflected to the boundary as the incident waves repeatedly. As a result, the reconstruction effect is weaker [23]. With the availability of large amount of data, it becomes applicable to utilize machine learning algorithms in the solution of the inverse problem of cavity. In recent years, machine learning methods have been widely employed in a variety of inverse problems and achieved favorable results. Li and Liu et al. [14] generated the inferred geometric body with the input characteristic parameters from the training dataset. In their study, the training dataset consists of some preprocessed body shapes associated with appropriately sampled characteristic parameters. This method applies the inverse scattering techniques in wave propagation theory to the body generation. This is based on a delicate one-to-one correspondence between a geometric body and the far-field pattern of a source scattering problem governed by the Helmholtz system. Yin et al. [31] proposed a two-layer sequence-to-sequence neural network, which can utilize phaseless far-field data to recover impenetrable obstacles, and they gave convergence results about the network. Aggarwal et al. [1] introduced a model-based image reconstruction framework with a convolution neural network (CNN) based on regularization prior. Their study proposed a model based deep learning (MoDL) framework, which combines the power of data-driven learning algorithms with that of the physics derived model-based framework. The MoDL framework provided a systematic approach to designing deep architectures for inverse problems with the arbitrary structure. Sanghvi et al. [27] introduced a

novel convolutional neural network structure, termed the contrast source network (CSN), to solve electromagnetic inverse scattering problems. The CSN is built on and extended the capability of existing physics-based inversion algorithms. Numerical experiments showed the CSN is capable of recovering high permittivity objects, which include homogeneous, heterogeneous and lossy scatterers. Proof of the convergence of neural network algorithms in machine learning can be found in [29, 30].

Machine learning has some unique advantages, such as the capability of finding potential rules and values from massive data, the power of quickly extracting data features, the strong parallel distribution processing ability, the application to approximating complex nonlinear relations, etc. This paper proposes a machine learning algorithm for the interior inverse scattering problem of the impenetrable cavity with the Dirichlet boundary condition. We consider the two-dimensional case, and reconstruct the shape of the cavity from the data of a single source and measurements located inside the cavity. Compared with the classic reconstruction methods, the present method has two major advantages. First, this method can still accurately reconstruct the shape of cavity when only small amount of measurements are available. Accuracy can be further improved with more measurement data. Second, in the limited-aperture case, this method has higher accuracy in the cavity shape reconstructed based on local near-field data. Finally, we would like to mention in passing that the study of inverse scattering problems with minimum/optimal measurement data has been a longstanding and intriguing topic in the literature; see e.g. [3, 4, 5, 7, 17, 18, 19, 20, 21, 26] and the references cited therein. Our study in this paper contributes to this topic for the interior scattering problem.

The rest of this paper is organized as follows. Section 2 introduces the inverse cavity scattering problem. In section 3, we establish the NSNN. The convergence of the NSNN is proved in section 4. In section 5, we conducted numerical experiments to illustrate the effectiveness of the NSNN. Finally, in section 6, we make conclusions and discuss some future works.

2. **The inverse scattering problem of the cavity.** Consider an impenetrable cavity $D \subset \mathbb{R}^2$, which is assumed to be a bounded simply connected domain with $\mathcal{C}^2$ boundary $\partial D$. Physically, we assume the medium inside $D$ is homogeneous with refractive index scaled to one. Let $\Gamma$ be a closed smooth curve inside the cavity (see figure 1). Consider the interior scattering problem of the Helmholtz equation for the cavity $D$, we find the scattered field $u^s \in C^2(D) \cap C(\overline{D})$ satisfying

$$\Delta u^s + k^2 u^s = 0, \quad \text{in } D, \tag{1}$$

$$u^s = -u^i, \qquad \text{on } \partial D, \tag{2}$$

where $k = \omega/c > 0$ is the wave number, $\omega > 0$ denotes the frequency of a time harmonic wave and $c > 0$ is the sound speed. The incident field $u^i$ is a point source of the form $u^i(x, z) = \Phi(x, z) = \frac{i}{4} H_0^{(1)}(k|x - z|)$, where $\Phi(x, z)$ is the fundamental solution to the Helmholtz equation, $H_0^{(1)}$ is the Hankel function of the first kind of order zero.

To ensure the uniqueness of the forward scattering problem 1-2, we have to assume that $k^2$ is not an interior eigenvalue of $-\Delta$ with respect to the boundary condition 2. Then, the well-posedness of the forward scattering problems 1-2 under the Dirichlet boundary condition can be proved (cf. [8]). Therefore, the forward scattering is to find the scattered field $u^s \in \epsilon H^1(D)$ such that $u^s$ solves the

Helmholtz equation 1 and the total field $u = u^i + u^s$ satisfies a boundary condition of the form 2.

Let $z$ be located at the closed smooth curve $\Gamma \subset D$. The inverse problem we are interested in is to determine the shape of $D$ from the measurement of the scattered field on the curve $\Gamma$ inside $D$ due to a point source located at $z \in \Gamma$. Under the restrictive assumptions on the size of the cavity, Qin and Cakoni [22] proved that the shape of the cavity can be uniquely determined by one source and several measurements.

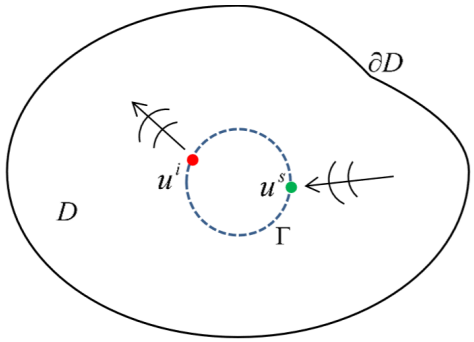


FIGURE 1. A schematic of the problem geometry.

3. **The inverse scattering network.** In this section, we present the architecture of the proposed neural network for the inverse problem. The inverse scattering problem of the cavity uses the known near-field data $u^s(x, z)$ to determine the shape of the cavity $D$. It is assumed that the observation curve $\Gamma \subset D$ is a circle, i.e., $\Gamma = \{\rho \in \mathbb{R}^2, |\rho| = r_\Gamma, r_\Gamma > 0\}$. Next, we introduce two notations for our subsequent use.

**Assumption 3.1.** *Let $D \subset \mathbb{R}^2$ be a bounded and simply connected domain with $\mathcal{C}^2$ boundary $\partial D$. We assume that the boundary curve of the cavity $D$ has the following parameterized representation:*

$$\partial D : f(\mathfrak{t}) = (f_1(\mathfrak{t}), f_2(\mathfrak{t})), 0 \le \mathfrak{t} \le 2\pi,$$

*where $f_1(\mathfrak{t})$ and $f_2(\mathfrak{t})$ admit the following (truncated) Fourier representations:*

$$\begin{cases} f_1(\mathfrak{t}) = a_0 + \sum\limits_{i=1}^{I} a_i \cos(i \cdot \mathfrak{t}) + \sum\limits_{i=1}^{I} b_i \sin(i \cdot \mathfrak{t}), \\ f_2(\mathfrak{t}) = c_0 + \sum\limits_{i=1}^{I} c_i \cos(i \cdot \mathfrak{t}) + \sum\limits_{i=1}^{I} d_i \sin(i \cdot \mathfrak{t}), \end{cases} \tag{3}$$

*where $I \in \mathbb{N}^+$. Let $Y = (y_1, y_2, \cdots, y_L)$ denote the ordered set of the Fourier coefficients $a_0, a_i, b_i, c_0, c_i, d_i, i = 1, 2, \cdots, I$, where $L = 4I + 2$, $y_l (l = 1, 2, \cdots, L)$ represents the $l$-th parameter in $Y$.*

**Definition 3.2.** The training data set $M$ of the near-field shape neural network (NSNN) is given by

$$M = \{u_i^s, Y_i; D_i \in \mathbb{D}\}_{i=1}^m, \tag{4}$$

where $m$ is the total amount of training data set $M$, $\mathbb{D}$ represents the set of the training shapes, $u_i^s = (x_1^i, x_2^i, \cdots, x_N^i) \in \mathbb{C}^N$ means the near-field data of $D_i$,

$x_n^i(n = 1, 2, \cdots, N)$ represents the measurement of the $n$-th observation point in $u_i^s$, $Y_i = (y_1^i, y_2^i, \cdots, y_L^i) \in \mathbb{R}^L$ means the true shape parameters of $D_i$, $y_l^i(l = 1, 2, \cdots, L)$ represents the value of $l$-th parameter in $Y_i$.

It is remarked that $\partial D$ parametrized of the form 3 is rather general, which includes the star-shaped domain as a special case. In fact, if $D$ is star-shaped, it can be parametrized as $r(\mathfrak{t})(\cos\mathfrak{t}, \sin\mathfrak{t})$, $\mathfrak{t} \in (0, 2\pi)$, where $r : [0, 2\pi] \mapsto \mathbb{R}_+$ is the radial function. By a direct verification, one can show that the truncated Fourier expansion of $r(\mathfrak{t})(\cos\mathfrak{t}, \sin\mathfrak{t})$ is of the general form 3. Furthermore, we convert the problem of using the $u^s(x, z)$ to determine the shape of the cavity $D$ into the problem of using the $u^s(x, z)$ to determine the shape parameters $Y = (y_1, y_2, \cdots, y_L)$ of the cavity $D$.

In the NSNN, $u_i^s$ in the training data set $M = \{u_i^s, Y_i\}_i^m$ is used as the input of the near-field layer, $Y_i$ is used as the input of the shape layer. Next, we present the main ingredients in constructing the NSNN, which consists of the near-field layer and the shape layer, where the near-field layer is composed of a self-attention sublayer and a feedforward neural network (FNN) sublayer, and the shape layer is composed of a masked self-attention sublayer, a near-field shape attention sublayer and a fully connected sublayer; see figure 2 for a schematic illustration of its working state.

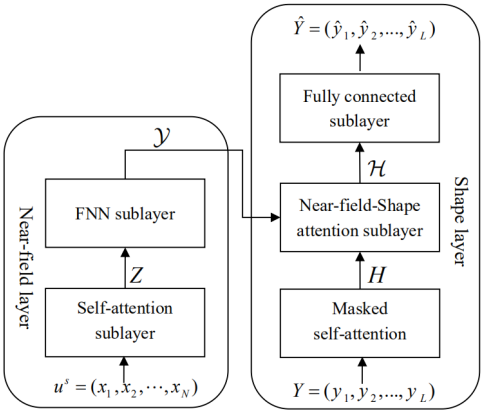


FIGURE 2. NSNN structure.

3.1. **Self-attention sublayer.** The self-attention sublayer learns the self-attention values of $x_1^i, x_2^i, \cdots, x_N^i$ in the near-field data $u_i^s = (x_1^i, x_2^i, \cdots, x_N^i)$ of the each input vector. Since the NSNN cannot handle complex numbers at this stage, let $x_1^i, x_2^i, \cdots, x_N^i$ be transformed to the real number field and conducting dimensional conversion. In order to explain the NSNN, we give two definitions as follow.

**Definition 3.3.** For $x_1^i = \iota_1^i + i\beta_1^i, x_2^i = \iota_2^i + i\beta_2^i, \cdots, x_N^i = \iota_N^i + i\beta_N^i (i = \sqrt{-1})$ in $u_i^s = (x_1^i, x_2^i, \cdots, x_N^i) \in \mathbb{C}^N$. Define a mapping $\mathcal{F} : \mathbb{C}^N \mapsto \mathbb{R}^O$, s.t.

$$\begin{cases} \mathcal{F}(x_1^i) := \widetilde{x}_1^i = \left[\iota_1^i; \beta_1^i; 0; \cdots; 0\right] \in \mathbb{R}^O, \\ \mathcal{F}(x_2^i) := \widetilde{x}_2^i = \left[0; 0; \iota_2^i; \beta_2^i; 0; \cdots; 0\right] \in \mathbb{R}^O, \\ \qquad\qquad \vdots \\ \mathcal{F}(x_N^i) := \widetilde{x}_N^i = \left[0; \cdots; 0_{N-1}; \iota_N^i; \beta_N^i; 0; \cdots; 0\right] \in \mathbb{R}^O. \end{cases}$$

**Definition 3.4.** Let $A = [a_1, a_2, \cdots, a_n] \in \mathbb{R}^n$, $B = \begin{pmatrix} b_{11} & b_{12} & \cdots & b_{1n} \\ b_{21} & b_{22} & \cdots & b_{2n} \\ \vdots & \vdots & \cdots & \vdots \\ b_{i1} & b_{i2} & \cdots & b_{mn} \end{pmatrix} \in \mathbb{R}^{m\times n}$, define a splice operator $\oplus_{i=1}^{n}$.

$$\oplus_{i=1}^{n} a_i = A,$$
$$\oplus_{i=1}^{m} \oplus_{j=1}^{n} b_{ij} = B.$$

First, input $u^s = (x_1, x_2, \cdots, x_N) \in \mathbb{C}^N$ into the self-attention sublayer, then get the vector $\widetilde{u}^s = (\widetilde{x}_1, \widetilde{x}_2, \cdots, \widetilde{x}_N) \in \mathbb{R}^O$ by mapping $\mathcal{F}$. Second, this sublayer will randomly generate three different learnable parameter matrices, $W_{en}^Q \in \mathbb{R}^{O\times O}, W_{en}^K \in \mathbb{R}^{O\times O}, W_{en}^V \in \mathbb{R}^{O\times O}$. Finally, the self-attention vectors of $\widetilde{x}_1$ is given by

$$\begin{cases} h_{11} = softmax\left[\frac{1}{\sqrt{O}}\left(\widetilde{x}_1 W_{en}^Q\right)\left(\widetilde{x}_1 W_{en}^K\right)^\top\right]\cdot\left(\widetilde{x}_1 W_{en}^V\right), h_{11} \in \mathbb{R}^O; \\ h_{12} = softmax\left[\frac{1}{\sqrt{O}}\left(\widetilde{x}_1 W_{en}^Q\right)\left(\widetilde{x}_2 W_{en}^K\right)^\top\right]\cdot\left(\widetilde{x}_2 W_{en}^V\right), h_{12} \in \mathbb{R}^O; \\ \quad\vdots \\ h_{1N} = softmax\left[\frac{1}{\sqrt{O}}\left(\widetilde{x}_1 W_{en}^Q\right)\left(\widetilde{x}_N W_{en}^K\right)^\top\right]\cdot\left(\widetilde{x}_N W_{en}^V\right), h_{1N} \in \mathbb{R}^O, \end{cases} \tag{5}$$

where $O$ is the number of nodes of the self-attention mechanism, softmax is the activation function [9], $\frac{1}{\sqrt{O}}$ is the scale factor. Similarly, the self-attention vectors $[(h_{21}, h_{22}, \cdots, h_{2N}), (h_{31}, h_{32}, \cdots, h_{3N}), \cdots, (h_{N1}, h_{N2}, \cdots, h_{NN})]$ of $(\widetilde{x}_2, \widetilde{x}_3, \cdots, \widetilde{x}_N)$ can be obtained by the formula 5. According to the operation rules given in Definition 3.4, the self-attention vectors are integrated to obtain the self-attention matrix $\hbar$.

$$\hbar = \oplus_{j=1}^{N} \oplus_{j=1}^{N} softmax\left[\frac{1}{\sqrt{O}}\left(\widetilde{x}_n W_{en}^Q\right)\left(\widetilde{x}_j W_{en}^K\right)^\top\right]\cdot\left(\widetilde{x}_j W_{en}^V\right), \hbar \in \mathbb{R}^{N\times N\cdot O}. \tag{6}$$

In order to extract more interactive information of the near-field data $u^s = (x_1, x_2, \cdots, x_N)$, let $\hbar$ act on the learnable linear projection matrix $W_0 \in \mathbb{R}^{N\cdot O\times O}$, the output $Z$ of this sublayer can be obtained.

$$Z = \hbar W_0, Z \in \mathbb{R}^{N\times O}. \tag{7}$$

3.2. **Feedforward neural network (FNN) sublayer.** Since the inverse problem is a typical nonlinear problem, the feedforward neural network (FNN) is used to provide the nonlinear transformation, so that the NSNN can better solve inverse problems. The FNN sublayer is shown in figure 3.

The FNN sublayer carries out the information transmission via the formula 8, for the input sequence $Z$, there is

$$\mathcal{Y} = \tanh\left(ZW_1 + b_1\right)W_2 + b_2, \mathcal{Y} \in \mathbb{R}^{N\times O}, \tag{8}$$

where $W_1 \in \mathbb{R}^{O\times\mathcal{O}}$ and $W_2 \in \mathbb{R}^{\mathcal{O}\times O}$ are the weight matrix of the first layer and the second layer respectively, $b_1$ and $b_2$ are the bias of the first layer and the bias of the second layer respectively. $O$ is the number of nodes in the self-attention mechanism, $\mathcal{O}$ is the number of neurons in the FNN sublayer, and $\tanh(\cdot)$ is the activation function [9].

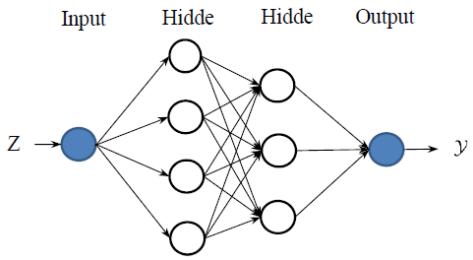


FIGURE 3. Feedforward neural network structure.

Next, the shape layer predicts the target sequence via regression. The input of shape layer is the true shape parameters $Y = (y_1, y_2, \cdots, y_L)$ and the output $\mathcal{Y}$ of the near-field layer. The output of the shape layer is the recovered shape parameters of cavity $\widehat{Y} = (\widehat{y}_1, \widehat{y}_2, \cdots, \widehat{y}_L)$, and the shape layer includes the following three sublayers.

3.3. **Masked self-attention sublayer.** In the masked self-attention sublayer, first of all, we add a positive constant $y_0$ to $Y = (y_1, y_2, \cdots, y_L) \in \mathbb{R}^L$ to get $Y = (y_0, y_1, y_2, \cdots, y_L) \in \mathbb{R}^{L+1}$, it is worth noting that the masked self-attention sublayer automatically mask the information of $y_{l+1}, y_{l+2}, \cdots, y_L$ when calculating the self-attention of $y_l (l = 0, 1, \cdots, L)$. Secondly, $\widetilde{Y} \in \mathbb{R}^{L+1}$ is obtained under the action of $\mathcal{F}(Y)$, and then three learnable parameters matrices $W_{de}^Q \in \mathbb{R}^{O\times O}, W_{de}^K \in \mathbb{R}^{O\times O}, W_{de}^V \in \mathbb{R}^{O\times O}$ are randomly generated in this layer. Finally, the self-attention matrix $H$ of $Y$ is obtained by the following formula.

$$H = \oplus_{i=0}^{l} softmax\left[\frac{1}{\sqrt{O}}\left(\widetilde{y}_i W_{de}^Q\right)\left(\widetilde{y}_l W_{de}^K\right)^\top\right] \cdot \left(\widetilde{y}_l W_{de}^V\right), l = 0, \cdots, L, H \in \mathbb{R}^{L\times O}. \tag{9}$$

3.4. **Near-field shape attention sublayer.** The input of this sublayer is $H \in \mathbb{R}^{L\times O}$ and the output $\mathcal{Y} \in \mathbb{R}^{N\times O}$ of the near-field layer. First, near-field shape attention sublayer initializes three learnable weight matrices $W_{ed}^Q \in \mathbb{R}^{O\times O}, W_{ed}^K \in \mathbb{R}^{O\times O}, W_{ed}^V \in \mathbb{R}^{O\times O}$. Then the attention matrix $\mathcal{H}$ of $H$ and $\mathcal{Y}$ is established by self-attention mechanism. Finally, $\mathcal{H}$ is input to the fully connected sublayer.

$$\mathcal{H} = softmax\left[\frac{1}{\sqrt{O}}\left(HW_{de}^Q\right)\left(\mathcal{Y}W_{de}^K\right)^\top\right] \cdot \left(\mathcal{Y}W_{de}^V\right), \mathcal{H} \in \mathbb{R}^O. \tag{10}$$

3.5. **Fully connected sublayer.** This sublayer performs affine transformation on $\mathcal{H}$, the reconstructed shape parameters $\widehat{Y}$ of the cavity are obtained by the following transformation.

$$\widehat{Y} = \mathcal{H}\mathcal{W} + \mathcal{B}, \tag{11}$$

where $\mathcal{W} \in \mathbb{R}^{O\times L}$ and $\mathcal{B} \in \mathbb{R}^L$ are respectively the weight and bias in the fully connected sublayer.

In the NSNN training process, the loss function is needed to judge the learning situation of the NSNN. The loss function used in this paper is given by Definition 4.3.

4. **Convergence analysis of the NSNN.** This section gives the convergence analysis and proof of the NSNN. The following definitions and assumptions will be used for our results.

**Definition 4.1.** Given an $m \times n$ matrix $A = (a_{ij})$, $vecA$ is defined as an $mn$ dimensional vector obtained by stacking the columns of the matrix $A$ on top of one another: $vecA = (a_{11}, a_{21}, \cdots, a_{m1}, a_{12}, a_{22}, \cdots, a_{m2}, \cdots, a_{1n}, a_{2n}, \cdots, a_{mn})^\top$.

**Definition 4.2.** We define the following activation function for any vector $A = (a_1, a_2, \cdots, a_n)$, $G(A) = (g(a_1), g(a_2), \cdots, g(a_n))^\top$, $S(A) = (s(a_1), s(a_2), \cdots, s(a_n))^\top$. Define

$$\begin{aligned} G'(A) &= (g'(a_1), g'(a_2), \cdots, g'(a_n))^\top, \\ S'(A) &= (s'(a_1), s'(a_2), \cdots, s'(a_n))^\top, \\ G''(A) &= (g''(a_1), g''(a_2), \cdots, g''(a_n))^\top, \\ S''(A) &= (s''(a_1), s''(a_2), \cdots, s''(a_n))^\top. \end{aligned}$$

To simplify the presentation, we write all the weights together as $W = (W^Q[W^Q_{en}, W^Q_{de}, W^Q_{ed}], W^K[W^K_{en}, W^K_{de}, W^K_{ed}], W^V[W^V_{en}, W^V_{de}, W^V_{ed}], W^O[W_0, W_1, W_2, \mathcal{W}])$, let $w = vecW$.

**Definition 4.3.** Let $\{Y_i\}_{i=1}^m$ be the true output of the NSNN and $\{\widehat{Y}_i\}_{i=1}^m$ be the predicted output of the NSNN. The loss function is defined as

$$E(w) = \frac{1}{2}\sum_{i=1}^{m}(Y_i - \widehat{Y}_i)^2, \tag{12}$$

where $m$ represents the total amount of training data sets, $Y_i$ represents true shape parameters of cavity of the $i$-th group, and $\widehat{Y}_i$ represents reconstructed shape parameters of cavity of the $i$-th group.

The gradient of the loss function 12 with respect to the weight $w$ is given by $\frac{\partial E}{\partial w} = -\sum\limits_{i=1}^{m}\left(Y_i - \widehat{Y}_i\right)\left(\frac{\partial \widehat{Y}_i}{\partial w}\right)^\top$. The gradient descent algorithm is used to update the weights and bias in NSNN. Starting from an arbitrary initial value $w^0$, the sequence of weights $\{w^t\}$ are constructed iteratively by

$$w^{t+1} = w^t + \Delta w, t = 0, 1, 2, \ldots, \tag{13}$$

where

$$\Delta w = -\alpha\frac{\partial E(w^t)}{\partial w} \tag{14}$$

and $\alpha > 0$ is the learning rate. We next introduce two assumptions in our study.

**Assumption 4.4.** *$|g(r)|, |g'(r)|, |g''(r)|$ and $|s(r)|, |s'(r)|, |s''(r)|$ are uniformly bounded for $r \in \mathbb{R}$.*

**Assumption 4.5.** *$\|w^t\|(t = 0, 1, 2, \ldots)$ is bounded in the learning process 13.*

**Remark 1.** Assumption 4.4 is valid for Sigmoid functions which are the most often used activation functions. An assumption like 4.5 is often used in the literature(see e.g.[29, 30]) for a nonlinear iteration procedure to guarantee the convergence.

**Theorem 4.6.** *Suppose that the loss function is given by the formula 12. The weight sequence $\{w^t\}$ is generated by the formula 13 for initial value $w^0$. Assumptions 4.4 and 4.5 are valid. Then, we have:*

*(1)* $E(w^{t+1}) \leq E(w^t)$;
*(2) There exists* $E^* \geq 0$ *such that* $\lim_{t\to+\infty} E(w^t) = E^*$.

Theorem 4.6 shows that the established NSNN is convergent. To prove Theorem 4.6, we first derive four auxiliary lemmas. In this proof, we use $C$ for a generic positive constant which may be different in different places, and assume that all biases $b = 0$ in the NSNN.

**Lemma 4.7.** *In the near-field shape attention sublayer has*

$$\mathcal{H} = s\left[\frac{1}{\sqrt{O}}(HW_{ed}^Q)\left(\mathcal{Y}W_{ed}^K\right)^\top\right]\cdot\left(\mathcal{Y}W_{ed}^V\right), \tag{15}$$

*where* $O \leq C$ *is a positive constant, let* $W_{ed}^Q, W_{ed}^K, W_{ed}^V$ *be* $W_Q, W_K, W_V$ *and* $\Delta\mathcal{H}(w^t) = \mathcal{H}(w^{t+1}) - \mathcal{H}(w^t)$, *if* $H$ *and* $\mathcal{Y}$ *are bounded, then* $\Delta\mathcal{H}(w^t) \leq C\|\Delta w^t\|$.

*Proof.* We only consider the case for $W_Q$ (The proof of the $W_K, W_V$ case is similar). The gradient of the loss function 12 relative to the weight $w^t$ in the near-field shape attention sublayer is given by

$$\frac{\partial E}{\partial w^t} = \frac{\partial E}{\partial \widehat{Y}}\frac{\partial \widehat{Y}}{\partial \mathcal{H}}\frac{\partial \mathcal{H}}{\partial W_Q^t} = -\sum_{i=1}^{M}\left(Y_i - \widehat{Y}_i\right)\mathcal{W}\frac{\partial \mathcal{H}}{\partial W_Q^t}, \tag{16}$$

where

$$\frac{\partial \mathcal{H}}{\partial W_Q^t} = s'\left[\frac{1}{\sqrt{O}}\left(HW_Q^t\right)\left(\mathcal{Y}W_K\right)^\top\right]\cdot\left(\mathcal{Y}W_V\right)\frac{1}{\sqrt{O}}H\left(\mathcal{Y}W_K\right)^\top. \tag{17}$$

Let

$$V(w^t) = \frac{1}{\sqrt{O}}\left(HW_Q^t\right)\left(\mathcal{Y}W_K\right)^\top, \tag{18}$$

then

$$\Delta V(w^t) = V(w^{t+1}) - V(w^t), \tag{19}$$

applying the Taylor expansion in the formula 19 yields

$$\begin{aligned}\Delta V(w^t) &= V(w^t) + V'(w^t)\Delta w^t + V''(\delta)(\Delta w^t)^2 - V(w^t)\\ &= V'(w^t)\Delta w^t + V''(\delta)(\Delta w^t)^2\\ &= \frac{1}{\sqrt{O}}H(\mathcal{Y}W_K)^\top\Delta w^t\\ &\leq C\|\Delta w^t\|,\end{aligned} \tag{20}$$

and each component of $\delta$ lies in between the two corresponding components of $w^t$ and $w^{t+1}$.

If $H$ and $\mathcal{Y}$ are bounded, noting the formulas 17, 18 and 20, we have

$$\begin{aligned}\Delta\mathcal{H}(w^t) &= \mathcal{H}(w^{t+1}) - \mathcal{H}(w^t)\\ &= s[V(w^t)]\mathcal{Y}W_V - s[V(w^t)]\mathcal{Y}W_V\\ &= s[V(w^t)]\mathcal{Y}W_V + s'[V(w^t)]\mathcal{Y}W_V\Delta V(w^t) + s''[\tau(w^t)]\mathcal{Y}W_V(\Delta V(w^t))^2\\ &\quad - s[V(w^t)]\mathcal{Y}W_V\\ &= s'[V(w^t)]\mathcal{Y}W_V\Delta V(w^t) + s''[\tau(w^t)]\mathcal{Y}W_V(\Delta V(w^t))^2\\ &\leq C\|\Delta w^t\|,\end{aligned}$$

where each component of $\tau(w^t)$ lies in between the two corresponding components of $V(w^t)$ and $V(w^{t+1})$. □

**Lemma 4.8.** *In the masked self-attention sublayer, we have*

$$H = \oplus_{i=0}^{l} s\left[\frac{1}{\sqrt{O}}\left(\widetilde{y}_i W_{de}^{Q}\right)\left(\widetilde{y}_l W_{de}^{K}\right)^{\top}\right]\cdot\left(\widetilde{y}_l W_{de}^{V}\right), l = 0, 1, \ldots, L, \tag{21}$$

*where $O \leq C$ is a positive constant, let $W_{de}^{Q}, W_{de}^{K}, W_{de}^{V}$ be $W_Q, W_K, W_V$ and $\Delta H(w^t) = H(w^{t+1}) - H(w^t)$, then we have $\Delta H(w^t) \leq C\|\Delta w^t\|$.*

*Proof.* We only consider the case for $W_Q$ (The proof of the $W_K, W_V$ case is similar). The gradient of the loss function 12 relative to the $w^t$ in the masked self-attention sublayer is given by

$$\begin{aligned}\frac{\partial E}{\partial w^t} &= \frac{\partial E}{\partial \widehat{Y}}\frac{\partial \widehat{Y}}{\partial \mathcal{H}}\frac{\partial \mathcal{H}}{\partial H}\frac{\partial H}{\partial W_Q^t} \\ &= -\sum_{i=1}^{M}\left(Y_i - \widehat{Y}_i\right)\mathcal{W}s'\left[\frac{1}{\sqrt{O}}\left(HW_{ed}^{Q}\right)\left(\mathcal{Y}W_{ed}^{K}\right)^{\top}\right] \\ &\cdot\left(\mathcal{Y}W_{ed}^{V}\right)\frac{1}{\sqrt{O}}W_{ed}^{Q}\left(\mathcal{Y}W_{ed}^{K}\right)^{\top}\frac{\partial H}{\partial W_Q^t},\end{aligned} \tag{22}$$

where

$$\frac{\partial H}{\partial W_Q^t} = \oplus_{i=0}^{l} s'\left[\frac{1}{\sqrt{O}}\left(\widetilde{y}_i W_Q^t\right)\left(\widetilde{y}_l W_K\right)^{\top}\right]\cdot\left(\widetilde{y}_l W_V\right)\frac{1}{\sqrt{O}}\widetilde{y}_i\left(\widetilde{y}_l W_K\right)^{\top}. \tag{23}$$

Let $U_{il}(w^t) = \frac{1}{\sqrt{O}}(\widetilde{y}_i W_Q^t)(\widetilde{y}_l W_V)^{\top}$, we have

$$\begin{aligned}\Delta U_{il}(w^t) &= U_{il}(w^{t+1}) - U_{il}(w^t) \\ &= U_{il}(w^t) + U_{il}'(w^t)\Delta w^t + U_{il}''(\vartheta)(\Delta w^t)^2 - U_{il}(w^t) \\ &= U_{il}'(w^t)\Delta w^t + U_{il}''(\vartheta)(\Delta w^t)^2 \\ &= \frac{1}{\sqrt{O}}\widetilde{y}_i(\widetilde{y}_l W_V)^{\top}\Delta w^t \\ &\leq C\|\Delta w^t\|,\end{aligned} \tag{24}$$

where each component of $\vartheta$ lies in between the two corresponding components of $w^t$ and $w^{t+1}$, by the formulas 23 and 24, we have

$$\begin{aligned}\Delta H(w^t) &= H(w^{t+1}) - H(w^t) \\ &= H(U_{il}(w^t)) + H'(U_{il}(w^t))\Delta U_{il}(w^t) + H''(\tau_{il}(w^t))(\Delta U_{il}(w^t))^2 \\ &- H(U_{il}(w^t)) \\ &= H'(U_{il}(w^t))\Delta U_{il}(w^t) + H''(\tau_{il}(w^t))(\Delta U_{il}(w^t))^2 \\ &\leq C\|\Delta w^t\|,\end{aligned}$$

where each component of $\tau_{il}(w^t)$ lies in between the two corresponding components of $U_{il}(w^t)$ and $U_{il}(w^{t+1})$ □

**Lemma 4.9.** *In the FNN sublayer, we have*

$$\mathcal{Y} = g(ZW_1 + b_1)W_2 + b_2, \tag{25}$$

*let $\Delta\mathcal{Y}(w^t) = \mathcal{Y}(w^{t+1}) - \mathcal{Y}(w^t)$, if $Z$ is bounded, then $\Delta\mathcal{Y}(w^t) \leq C\|\Delta w^t\|$, where $O \leq C$ is a positive constant.*

*Proof.* We only consider the case for $W_1$ (The proof of the $W_2$ case is similar). The gradient of the loss function 12 relative to the $w^t$ in the FNN sublayer is given by

$$\begin{aligned}\frac{\partial E}{\partial w^t} &= \frac{\partial E}{\partial \widehat{Y}}\frac{\partial \widehat{Y}}{\partial \mathcal{H}}\frac{\partial \mathcal{H}}{\partial \mathcal{Y}}\frac{\partial \mathcal{Y}}{\partial W_1^t} \\ &= -\sum_{i=1}^{m}\left(Y_i-\widehat{Y}_i\right)\mathcal{W}\left[s'\left[\frac{1}{\sqrt{O}}\left(HW_{ed}^Q\right)\left(\mathcal{Y}W_{ed}^K\right)^\top\right]\left(HW_{ed}^Q\right)W_{ed}^K\left(\mathcal{Y}W_{ed}^V\right)\right. \\ &\left. + s\left[\frac{1}{\sqrt{O}}\left(HW_{ed}^Q\right)\left(\mathcal{Y}W_{ed}^K\right)^\top\right]W_{ed}^V\right]\frac{\partial \mathcal{Y}}{\partial W_1^t},\end{aligned} \tag{26}$$

where

$$\frac{\partial \mathcal{Y}}{\partial W_1^t} = g'(ZW_1^t + b_1)W_2 Z. \tag{27}$$

Let $\Delta\mathcal{Y}(w^t) = \mathcal{Y}(w^{t+1}) - \mathcal{Y}(w^t)$, if $Z$ is bounded, then from the formula 27 we can get

$$\begin{aligned}\Delta\mathcal{Y}(w^t) &= \mathcal{Y}(w^{t+1}) - \mathcal{Y}(w^t) \\ &= \mathcal{Y}(w^t) + \mathcal{Y}'(w^t)\Delta w^t + \mathcal{Y}''(\kappa)(\Delta w^t)^2 - \mathcal{Y}(w^t) \\ &= \mathcal{Y}'(w^t)\Delta W_1^t + \mathcal{Y}''(\kappa)(\Delta w^t)^2 \\ &\le C\|\Delta w^t\|,\end{aligned}$$

where each component of $\kappa$ lies in between the two corresponding components of $\mathcal{Y}(w^t)$ and $\mathcal{Y}(w^{t+1})$. □

**Lemma 4.10.** *In the self-attention sublayer, we have*

$$\hbar = \oplus_{j=1}^{N}\oplus_{n=1}^{N} s\left[\frac{1}{\sqrt{O}}\left(\widetilde{x}_n W_{en}^Q\right)\left(\widetilde{x}_j W_{en}^K\right)^\top\right]\cdot\left(\widetilde{x}_j W_{en}^V\right); \tag{28}$$

$$Z = hW_0, \tag{29}$$

*where $O \le C$ is a positive constant, let $W_{en}^Q, W_{en}^K, W_{en}^V$ be $W_Q, W_K, W_V$ and $\Delta\hbar(w^t) = \hbar(w^{t+1}) - \hbar(w^t)$, then we have $\Delta\hbar(w^t) \le C\|\Delta w^t\|$ and $\Delta Z(w^t) \le C\|\Delta w^t\|$.*

*Proof.* We only consider the case for $W_Q$ (The proof of the $W_K, W_V$ case is similar). The gradient of the loss function 12 relative to the $w^t$ in the self-attention sublayer is given by

$$\begin{aligned}\frac{\partial E}{\partial w^t} &= \frac{\partial E}{\partial \widehat{Y}}\frac{\partial \widehat{Y}}{\partial \mathcal{H}}\frac{\partial \mathcal{H}}{\partial \mathcal{Y}}\frac{\partial \mathcal{Y}}{\partial Z}\frac{\partial Z}{\partial \hbar}\frac{\partial \hbar}{\partial W_Q^t} \\ &= -\sum_{i=1}^{m}\left(Y_i-\widehat{Y}_i\right)\mathcal{W}\left[s'\left[\frac{1}{\sqrt{O}}\left(HW_{ed}^Q\right)\left(\mathcal{Y}W_{ed}^K\right)^\top\right]\left(HW_{ed}^Q\right)\left(W_{ed}^K\right)\mathcal{Y}W_{ed}^V\right. \\ &\left. + s\left[\frac{1}{\sqrt{O}}\left(HW_{ed}^Q\right)\left(\mathcal{Y}W_{ed}^K\right)^\top\right]W_{ed}^V\right]g'\left(ZW_1+b_1\right)W_2W_1W_0\frac{\partial \hbar}{\partial W_Q^t};\end{aligned} \tag{30}$$

$$\begin{aligned}\frac{\partial E}{\partial w^t} &= \frac{\partial E}{\partial \widehat{Y}}\frac{\partial \widehat{Y}}{\partial \mathcal{H}}\frac{\partial \mathcal{H}}{\partial \mathcal{Y}}\frac{\partial \mathcal{Y}}{\partial Z}\frac{\partial Z}{\partial W_0^t} \\ &= -\sum_{i=1}^{m}\left(Y_i-\widehat{Y}_i\right)\mathcal{W}\Bigg[s'\left[\frac{1}{\sqrt{O}}\left(HW_{ed}^{Q}\right)\left(\mathcal{Y}W_{ed}^{K}\right)^{\top}\right]\left(HW_{ed}^{Q}\right)\left(W_{ed}^{K}\right)\mathcal{Y}W_{ed}^{V} \\ &+ s\left[\frac{1}{\sqrt{O}}\left(HW_{ed}^{Q}\right)\left(\mathcal{Y}W_{ed}^{K}\right)^{\top}\right]W_{ed}^{V}\Bigg]g'\left(ZW_1+b_1\right)W_2W_1\frac{\partial Z}{\partial W_0^t},\end{aligned} \tag{31}$$

where

$$\frac{\partial \hbar}{\partial W_Q^t} = \oplus_{j=1}^{N}\oplus_{n=1}^{N} s'\left[\frac{1}{\sqrt{O}}\left(\widetilde{x}_nW_Q^t\right)\left(\widetilde{x}_jW_K\right)^{\top}\right]\frac{1}{\sqrt{O}}\widetilde{x}_n\left(\widetilde{x}_jW_K\right)^{\top}\left(\widetilde{x}_jW_V\right); \tag{32}$$

$$\frac{\partial Z}{\partial W_0^t} = \hbar. \tag{33}$$

Let $B_{nj}(w^t) = \frac{1}{\sqrt{O}}\left(\widetilde{x}_nW_Q^t\right)\left(\widetilde{x}_jW_K\right)^{\top}$, we have

$$\begin{aligned}\Delta B_{nj}(w^t) &= B_{nj}(w^{t+1}) - B_{nj}(w^t) \\ &= B_{nj}(w^t) + B'_{nj}(w^t)\Delta w^t + B''_{nj}(\gamma)(\Delta w^t)^2 - B_{nj}(w^t) \\ &= B'_{nj}(w^t)\Delta w^t + B''_{nj}(\gamma)(\Delta w^t)^2 \\ &= \frac{1}{\sqrt{O}}\widetilde{x}_n(\widetilde{x}_jW_K)^{\top}\Delta w^t \\ &\le C\|\Delta w^t\|,\end{aligned} \tag{34}$$

where each component of $\gamma$ lies in between the two corresponding components of $w^t$ and $w^{t+1}$.

Let $\Delta\hbar(B_{nj}(w^t)) = \hbar(B_{nj}(w^{t+1})) - \hbar(B_{nj}(w^t))$. By the formulas 30, 32 and 34, we can get

$$\begin{aligned}\Delta\hbar(B_{nj}(w^t)) &= \hbar(B_{nj}(w^{t+1})) - \hbar(B_{nj}(w^t)) \\ &= \hbar(B_{nj}(w^t)) + \hbar'(B_{nj}(w^t))(\Delta B_{nj}w^t)) + \hbar''(\nu_{nj}(w^t))(\Delta B_{nj}(w^t))^2 \\ &- \hbar(B_{nj}(w^t)) \\ &= \oplus_{j=1}^{N}\oplus_{n=1}^{N} s'\left[B_{nj}(w^t)\right](\widetilde{x}_jW_V)(\Delta B_{nj}(w^t)) \\ &+ \oplus_{j=1}^{N}\oplus_{n=1}^{N} s''\left[\nu_{nj}(w^t)\right](\widetilde{x}_jW_V)(\Delta B_{nj}(w^t))^2 \\ &\le C\|\Delta w^t\|,\end{aligned} \tag{35}$$

where each component of $\nu_{nj}(w^t)$ lies in between the two corresponding components of $B_{nj}(w^t)$ and $B_{nj}(w^{t+1})$. □

Let $\Delta Z(w^t) = Z(w^{t+1}) - Z(w^t)$, suppose that Assumption 4.4 and Assumption 4.5 are satisfied, from the formulas 31, 33 and 35 we have $\Delta Z(w^t) \le C\|\Delta w^t\|$.

*Proof of Theorem 4.6.* Applying the Taylor expansion, together with the use of the formulas 14, 16, 17, 22, 23, 26, 27, 30, 32, 35 and Lemma 4.7, 4.8, 4.9 and Lemma

4.10, we have

$$
\begin{aligned}
E(w^{t+1}) - E(w^t) = & -\sum_{i=1}^{m}\left(Y_i - \widehat{Y}_i\left(w^t\right)\right)^2 \frac{\partial \widehat{Y}}{\partial w}\|\Delta w^t\| \\
& -\frac{1}{2}\sum_{i=1}^{m}\left(Y_i - \widehat{Y}_i\left(w^t\right)\right)\frac{\partial^2 \widehat{Y}}{\partial w^2}\|\Delta w^t\|^2 \\
& = -\sum_{i=1}^{m}\left(Y_i - \widehat{Y}_i\left(w^t\right)\right)\mathcal{W}\left[s'\left[\frac{1}{\sqrt{O}}\left(HW_{ed}^{Q}\right)\left(\mathcal{Y}W_{ed}^{K}\right)^{\top}\right]\left(HW_{ed}^{Q}\right)W_{ed}^{K}\right. \\
& \left.\cdot\left(\mathcal{Y}W_{ed}^{V}\right) + s\left[\frac{1}{\sqrt{O}}\left(HW_{ed}^{Q}\right)\left(\mathcal{Y}W_{ed}^{K}\right)^{\top}\right]W_{ed}^{V}\right] g'\left(ZW_1 + b_1\right)W_2W_1 \\
& \cdot W_0 \oplus_{j=1}^{N}\oplus_{n=1}^{N} s'\left[\frac{1}{\sqrt{O}}\left(\widetilde{x}_nW_{en}^{Q}\right)\left(\widetilde{x}_jW_{en}^{K}\right)^{\top}\right]\frac{1}{\sqrt{O}}\widetilde{x}_n\left(\widetilde{x}_jW_{en}^{K}\right)^{\top}\left(\widetilde{x}_jW_{en}^{V}\right) \\
& \cdot\|\Delta w^t\| - \frac{1}{2}\sum_{i=1}^{m}\left(Y_i - \widehat{Y}_i\left(w^t\right)\right)\left[s'\left[\frac{1}{\sqrt{O}}\left(HW_{ed}^{Q}\right)\left(\mathcal{Y}W_{ed}^{K}\right)^{\top}\right]\left(HW_{ed}^{Q}\right)\right. \\
& \left.\cdot\left(W_{ed}^{K}\right)\mathcal{Y}W_{ed}^{V} + s\left[\frac{1}{\sqrt{O}}\left(HW_{ed}^{Q}\right)\left(\mathcal{Y}W_{ed}^{K}\right)^{\top}\right]W_{ed}^{V}\right] g'\left(ZW_1 + b_1\right)W_2W_1 \\
& \cdot W_0 \oplus_{j=1}^{N}\oplus_{n=1}^{N} s''\left[\upsilon\left(\frac{1}{\sqrt{O}}\left(\widetilde{x}_nW_{en}^{Q}\right)\left(\widetilde{x}_jW_{en}^{K}\right)^{\top}\right)\right]\frac{1}{\sqrt{O}}\widetilde{x}_n\left(\widetilde{x}_jW_{en}^{K}\right)^{\top} \\
& \cdot\left(\widetilde{x}_jW_{en}^{V}\right)\|\Delta w^t\|^2 \\
& \leq -\frac{1}{\alpha}\|\Delta w^t\|^2 + \rho\left(\Delta w^t\right),
\end{aligned}
\tag{36}
$$

where each component of $\upsilon\left(\frac{1}{\sqrt{O}}\left(\widetilde{x}_nW_{en}^{Q}\right)\left(\widetilde{x}_jW_{en}^{K}\right)^{\top}\right)$ lies in between the two corresponding components of $\upsilon\left(w^{t+1}\right)$ and $\upsilon\left(w^t\right)$.

By Assumption 4.4, Assumption 4.5, Lemma 4.7, Lemma 4.8, Lemma 4.9, Lemma 4.10 and the Cauchy-Schwarz inequality, we get

$$
\rho(\Delta w^t) \leq C\|\Delta w^t\|^2. \tag{37}
$$

A combination of the formulas 36 and 37 leads to

$$
E\left(w^{t+1}\right) - E\left(w^t\right) \leq -\left(\frac{1}{\alpha} - C\right)\|\Delta w^t\|^2. \tag{38}
$$

Hence, the conclusion (1) in Theorem 4.6 is valid if the learning rate is small enough such that $0 < \alpha < \frac{1}{C}$, where $C$ is the constant in the formula 38. Since the nonnegative sequence $\{E(w^t)\}$ is monotone and bounded below, there must exist a limiting value $E^* \geq 0$ such that $\lim_{t\to+\infty} E(w^t) = E^*$. So the conclusion (2) in Theorem 4.6 is proved. □

## 5. Numerical experiments.

In this section, we present several typical numerical experiments to demonstrate the effectiveness and efficiency of the proposed the NSNN for the inverse cavity scattering problem.

5.1. **Data processing.** First, we recall that the training data set $M$ in Definition 3.2, where $u_i^s$ and $Y_i$ represent the near-field data and the truncated Fourier-shape vector associated with a cavity. Furthermore, for a given shape of cavity, the existence of a solution to the interior Dirichlet problem of the cavity can be based on boundary integral equations. Hence, for the forward cavity scattering problem, we make use of the integral equation method for solving 1-2 to obtain the associated near-field data (cf. [8]). Second, in order to ensure the uniqueness of the inverse cavity scattering problem, we need to restrict the size of the cavity (cf.[22]). Therefore, $\mathbb{D}$ is constructed according to 3 by varying the Fourier coefficients in $[-\varrho, \varrho]$ in a uniformly distributed manner by excluding those self-intersecting boundary curves, where $\varrho \in \mathbb{R}_+$ is an a-priori given constant. Next, we fix $I$ in 3, and classify the shapes of the cavity according to the corresponding Fourier-shape parameters and near-field data, and label each category accordingly, and then each labeled category is used as the training data of the naive Bayesian classifier (NBC) to train the NBC network.

That is, in the first phase, for a given set of the near-field data, we can determine the suitable category to which the associated cavity should belong. In the second phase, within a given class of cavities, we train the NSNN to recover the corresponding Fourier coefficients of an unknown cavity by given its near-field data.

5.2. **Shape reconstruction.** For all examples, we set the radius $r_\Gamma = 0.5$ and center $o_\Gamma = (0, 0)$ of the detection circle $\Gamma$ inside the cavity, the single point source position is $z = (0.5, 0)$, the wavenumber is $k = 1.5$, the number of observation points is $N$, the limited-aperture range is $\mathcal{P}$. Unless otherwise specified in the following experiments, the parameter values of the NSNN are shown in Table 1. The values of learning rate $\alpha$, dropout, $O$ and $\mathcal{O}$ are derived from the reference [9], the values of the other parameters are obtained through multiple experiments. The influence of the value of the experimental parameters on the experimental results will be taken as the next step. We use "$-$" to indicate the true shape of the cavity, and "$--$" to indicate the reconstructed shape of the cavity.

TABLE 1. Parameter values of the NSNN.

| Parameter | value |
|---|---|
| The Near-field shape of layer | 2 |
| Learning rate $\alpha$ | 0.0001 |
| Dropout | 0.5 |
| O | 256 |
| $\mathcal{O}$ | 256 |
| Batch | 1000 |
| Epoch: $t$ | 100 |

**Example 1.** Reconstruct the cavity with different numbers of observation points.

In this experiment, the number of training cavities is set to be $m = 50000$, the limited-aperture range is set to be $\mathcal{P} = [0, 2\pi]$, the number of observation points for the kite-shaped cavity and the peanut-shaped cavity is set to be $N = 5, 7, 9$ respectively, the number of observation points for the starfish-shaped cavity is set to be $N = 5, 11, 19$ respectively. There is no noise in the near-field data, and the reconstruction result is shown in figure 4.

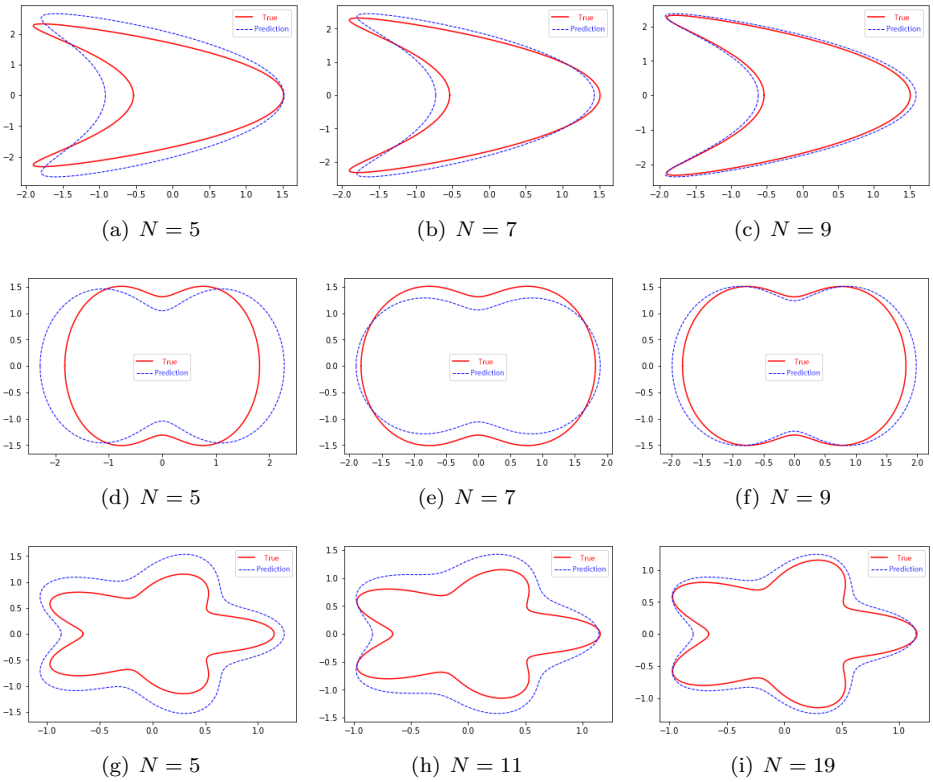


(a) $N = 5$ (b) $N = 7$ (c) $N = 9$

(d) $N = 5$ (e) $N = 7$ (f) $N = 9$

(g) $N = 5$ (h) $N = 11$ (i) $N = 19$

FIGURE 4. Reconstruct three shapes of cavity under the conditions of single point source incidence and limited observation points.

Figure 4 shows the reconstructed effects of the kite-shaped cavity, the peanut-shaped cavity and the starfish-shaped cavity, respectively. Among them, the kite-shaped cavity figure 4(a), (b), (c) and the peanut-shaped cavity figure 4(d), (e), (f) from left to right represent the number of observation points of $N = 5$, $N = 7$ and $N = 9$, respectively. The starfish-shaped cavity figure 4(g), (h) and (i) from left to right represent the number of observation points of $N = 5$, $N = 11$ and $N = 19$. It can be seen that when the total number of training data sets and the epoch of train remain unchanged, as the number of observation points increases, the near-field data will increase, then the feature information about the cavity by the NSNN will be extracted more, and the shape of the cavity will be reconstructed more accurately. For the kite-shaped cavity and the peanut-shaped cavity, the better effect of reconstruction can be achieved when the number of observation points is $N = 9$, while for the starfish-shaped cavity with more parameters, the better effect of reconstruction can be achieved when the number of observation points increases to $N = 19$. Therefore, the reconstruction effect of the NSNN is affected by the complexity of the shape of cavity. The more parameters, the more complex the shape of the cavity, and the effect of reconstruction becomes worse. In the experiment, we can improve the effect of reconstruction by increasing the number of observation points.

**Example 2.** Reconstruct the cavity with the near-field data containing different noise levels.

We consider adding noise levels of noise $= 0\%, 5\%, 10\%$, and $20\%$ to the real and the imaginary parts of the near-field data of the kite-shaped cavity, the peanut-shaped cavity and the starfish-shaped cavity, respectively (Here, the noise is chosen to be Gaussian white noise with mean being 0 and variance being 0.05, 0.1 and 0.2, respectively.). Set $m = 50000$, $\mathcal{P} = [0, 2\pi]$, the number of observation points for the kite-shaped cavity and the peanut-shaped cavity is set to be $N = 9$, the number of observation points for the starfish-shaped cavity is set to be $N = 19$. The reconstruction effect of the kite-shaped cavity is shown in figure 5, the reconstruction effect of the peanut-shaped cavity is shown in figure 6 and the reconstruction effect of the starfish-shaped cavity is shown in figure 7.

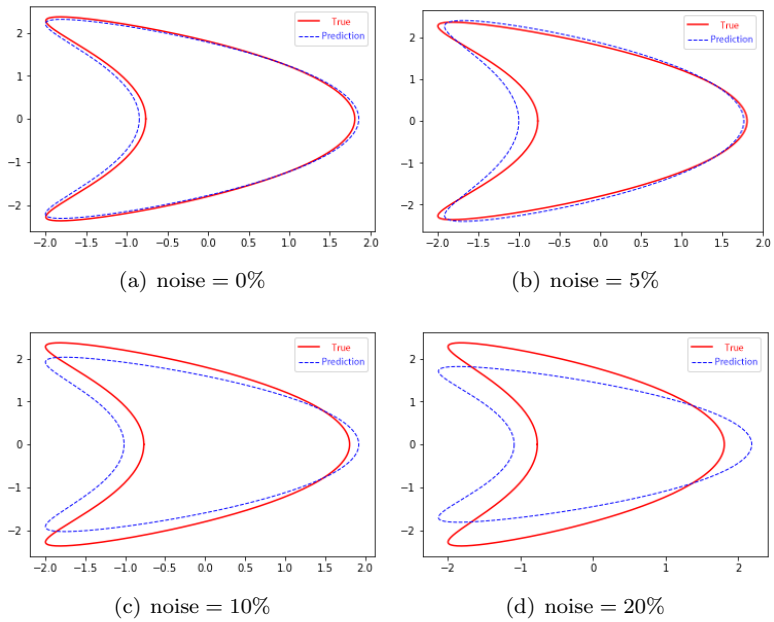


(a) noise $= 0\%$ (b) noise $= 5\%$

(c) noise $= 10\%$ (d) noise $= 20\%$

FIGURE 5. Reconstruct the kite-shaped cavity with different noises.

It can be seen from figure 5, 6, and 7 that when the noise level is below 10%, the noise has little effect on the reconstruction of the NSNN. Of course, the results of the reconstruction deteriorate as the noise level increases. When the noise is increased to 20%, the results of the NSNN reconstruction will deviate obviously from the true boundary of the cavity. Due to the fact that the number of shape parameters of the starfish-shaped cavity is relatively larger and the noise exists in the near-field data, the NSNN is more complex to extract the information of near field data and shape parameters, which leads to the poor effect of the NSNN reconstruction.

**Example 3.** Reconstruct the cavity with difference of the total number of training data sets.

We observe the reconstruction effect of the NSNN by changing the total amount $m$ of training data set. Taking the kite-shaped cavity as an example, the number of training cavities is set to be $m = 10000$, $m = 30000$, $m = 50000$, respectively.

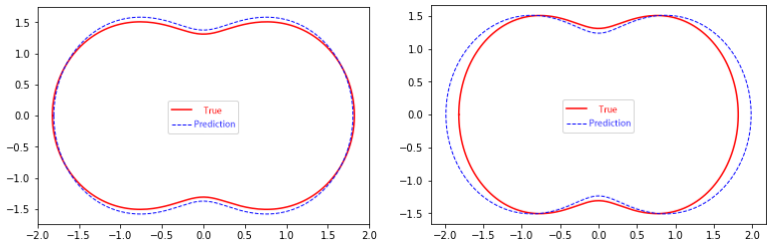


(a) noise = 0% (b) noise = 5%

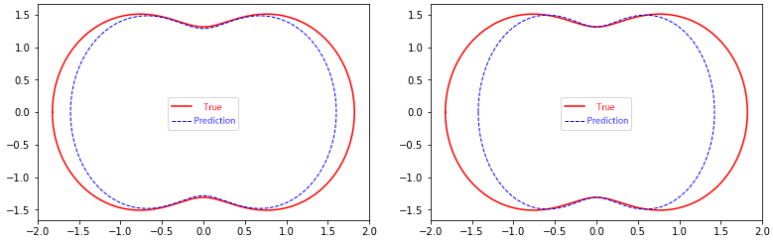


(c) noise = 10% (d) noise = 20%

FIGURE 6. Reconstruct the peanut-shaped cavity with different noises.

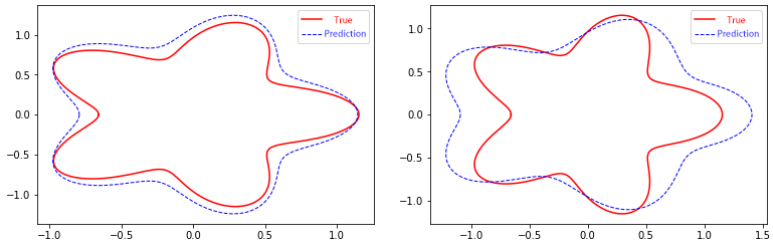


(a) noise = 0% (b) noise = 5%

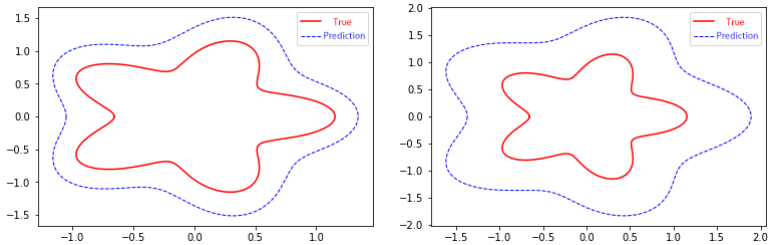


(c) noise = 10% (d) noise = 20%

FIGURE 7. Reconstruct the starfish-shaped cavity with different noises.

Set $\mathcal{P} = [0, 2\pi]$ and $N = 9$, the near-field data has no noise, and the reconstruction effect is shown in figure 8.

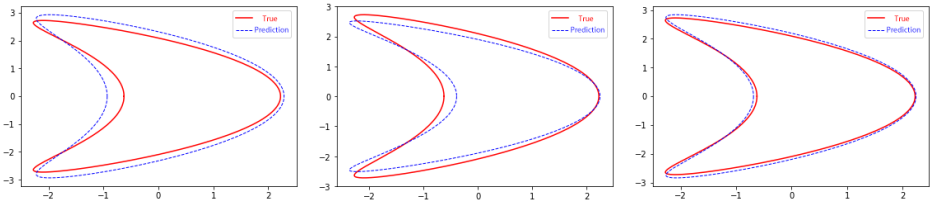


(a) $m = 10000$ (b) $m = 30000$ (c) $m = 50000$

FIGURE 8. Reconstruct the kite-shaped cavity under different $m$.

From the figure 8, we can see that as $m$ gradually increases, the effect of reconstruction is improved gradually, thereby the reconstructed shape of cavity is closer to the true shape of cavity.

In the above experiments, the shape of the cavity was reconstructed at the full-aperture range, namely $\mathcal{P} = [0, 2\pi]$, and the effect of reconstruction is ideal. In order to make the experiment closer to the actual situation. In Example 4, we consider reconstructing the shape of the cavity with the limited-aperture.

**Example 4.** Reconstruction of cavity with different local scattering data.

We consider the reconstruction by the NSNN when the limited-aperture range is set to be $\mathcal{P} = \left[\frac{3\pi}{4}, \frac{5\pi}{4}\right]$ , $\left[\frac{\pi}{2}, \frac{3\pi}{2}\right]$, $[0, 2\pi]$ respectively. This experiment takes the kite-shaped cavity as an example, set $m = 50000$ and $N = 9$. The near-field data has no noise, and the effect of reconstruction is shown in figure 9.

It can be seen from figure 9 that as the limited-aperture range gradually decreases, the effect of reconstruction will deteriorate accordingly. This is because when the limited-aperture range $\mathcal{P}$ is reduced, the similarity between the near-field data increases, resulting in the available cavity information from the near-field data becomes less and less, which suppresses the accuracy of reconstruction. However, we can see that the NSNN can also reconstruct the shape of the cavity well under the limited-aperture range.

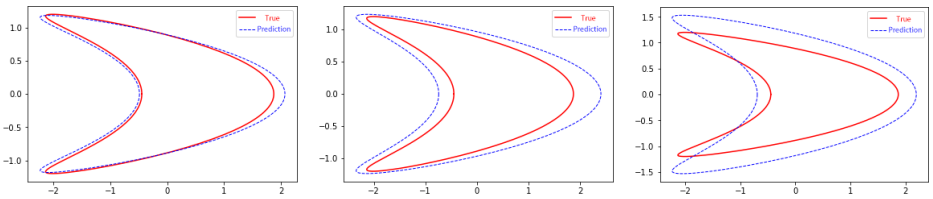


(a) $\mathcal{P} = [0, 2\pi]$ (b) $\mathcal{P} = \left[\frac{\pi}{2}, \frac{3\pi}{2}\right]$ (c) $\mathcal{P} = \left[\frac{3\pi}{4}, \frac{5\pi}{4}\right]$

FIGURE 9. Reconstruct the kite-shaped cavity under different the limited-aperture range conditions.

6. **Conclusions.** In this paper, we propose the NSNN to solve the interior inverse scattering problems connected with the Helmholtz equation, and we prove the convergence of the NSNN. Numerical experiments show that the NSNN can well reconstruct the shape of the cavity by using a single point source and a few observation points. The experimental results also confirm the generalization ability and robustness of this method. However, there are still many problems need to be further studied, such as the influence of the selection of the NSNN parameters on the effect of the NSNN reconstruction. In the future, we would like to extend the study to three dimensional problems and the inverse cavity electromagnetic scattering problems governed by the Maxwell system.

**Acknowledgments.** The work of Weishi Yin was supported by a startup fund from National Natural Science Foundation of China (project 11671107).

## REFERENCES

[1] H. K. Aggarwal, M. P. Mani and M. Jacob, MoDL: Model based deep learning architecture for inverse problems, *IEEE Transactions on Medical Imaging*, **38** (2019), 394–405.
[2] M. N. Akinci, Detection of the cavities inside a target with near field orthogonality sampling method, *2018 18th Mediterranean Microwave Symposium (MMS)*, IEEE, (2018), 391–393.
[3] G. Alessandrini and L. Rondi, Determining a sound-soft polyhedral scatterer by a single far-field measurement, *Proc. Amer. Math. Soc.*, **133** (2005), 1685–1691.
[4] E. Blåsten and H. Liu, On corners scattering stably, nearly non-scattering interrogating waves, and stable shape determination by a single far-field pattern, preprint, arXiv:1611.03647.
[5] E. Blåsten and H. Liu, Recovering piecewise constant refractive indices by a single far-field pattern, preprint, arXiv:1705.00815.
[6] F. Cakoni, D. Colton and S. Meng, The inverse scattering problem for a penetrable cavity with internal measurements, *AMS Contemporary Mathematics*, **615** (2014), 71–88.
[7] J. Cheng and M. Yamamoto, Uniqueness in an inverse scattering problem within non-trapping polygonal obstacles with at most two incoming waves, *Inverse Problems*, **19** (2003), 1361–1384.
[8] D. Colton and R. Kress, *Inverse Acoustic and Electromagnetic Scattering Theory*, $4^{nd}$ edition, Applied Mathematical Sciences, 93. Springer, Cham, New York, 2019.
[9] L. Goodfellow, Y. Bengio and A. Courville, *Deep Learning*, MIT Press, London, 2017.
[10] J. Guo, Q. Yang, M. Cai, G. Yan and Z. Guo, Reconstruction of a crack with the incident waves and measurements inside a penetrable cavity, *J. Inverse Ill-Posed Probl.*, **27** (2019), 643–656.
[11] Y. Hu, F. Cakoni and J. Liu, The inverse scattering problem for a partially coated cavity with interior measurements, *Appl. Anal.*, **93** (2014), 936–956.
[12] P. Jakubik and R. Potthast, Testing the integrity of some cavity-the Cauchy problem and the range test, *Appl. Numer. Math.*, **58** (2008), 899–914.
[13] A. Karageorghis, D. Lesnic and L. Marin, The method of fundamental solutions for the identification of a scatterer with impedance boundary condition in interior inverse acoustic scattering, *Eng. Anal. Bound. Elem.*, **92** (2018), 218–224.
[14] J. Li, H. Liu, W.-Y. Tsui and X. Wang, An inverse scattering approach for geometric body generation: A machine learning perspective, *Mathematics in Engineering*, **1** (2019), 800–823.
[15] P. Li and Y. Wang, Near-field imaging of interior cavities, *Commun. Comput. Phys.*, **17** (2015), 542–563.
[16] X. Liu, The factorization method for cavities, *Inverse Problems*, **30** (2014), 015006, 18 pp.
[17] H. Liu, A global uniqueness for formally determined inverse electromagnetic obstacle scattering, *Inverse Problems*, **24** (2008), 035018, 13 pp.
[18] H. Liu, M. Petrini, L. Rondi and J. Xiao, Stable determination of sound-hard polyhedral scatterers by a minimal number of scattering measurements, *J. Differential Equations*, **262** (2017), 1631–1670.
[19] H. Liu, L. Rondi and J. Xiao, Mosco convergence for $H(\mathrm{curl})$ spaces, higher integrability for Maxwell's equations, and stability in direct and inverse EM scattering problems, *J. Eur. Math. Soc. (JEMS)*, **21** (2019), 2945–2993.

[20] H. Liu and J. Zou, Uniqueness in an inverse acoustic obstacle scattering problem for both sound-hard and sound-soft polyhedral scatterers, *Inverse Problems*, **22** (2006), 515–524.
[21] H. Liu and J. Zou, On unique determination of partially coated polyhedral scatterers with far field measurements, *Inverse Problems*, **23** (2007), 297–308.
[22] H. Qin and F. Cakoni, Nonlinear integral equations for shape reconstruction in the inverse interior scattering problem, *Inverse Problems*, **27** (2011), 035005, 17 pp.
[23] H. Qin and D. Colton, The inverse scattering problem for cavities, *Appl. Numer. Math.*, **62** (2012), 699–708.
[24] H. Qin and D. Colton, The inverse scattering problem for cavities with impedance boundary condition, *Adv. Comput. Math.*, **36** (2012), 157–174.
[25] F. Qu, J. Yang and H. Zhang, Shape reconstruction in inverse scattering by an inhomogeneous cavity with internal measurements, *SIAM J. Imaging Sci.*, **12** (2019), 788–808.
[26] L. Rondi, Stable determination of sound-soft polyhedral scatterers by a single measurement, *Indiana Univ. Math. J.*, **57** (2008), 1377–1408.
[27] Y. Sanghvi, Y. Kalepu and U. K. Khankhoje, Embedding deep learning in inverse scattering problems, *IEEE Transactions on Computational Imaging*, **6** (2020), 46–56.
[28] Y. Sun, Y. Guo and F. Ma, The reciprocity gap functional method for the inverse scattering problem for cavities, *Appl. Anal.*, **95** (2016), 1327–1346.
[29] D. Xu, Z. Li and W. Wu, Convergence of gradient method for a fully recurrent neural network, *Soft Computing*, **14** (2010), 245–250.
[30] D. Xu, Z. Li, W. Wu, X. Ding and D. Qu, Convergence of gradient descent algorithm for a recurrent neuron, *International Symposium on Neural Networks*, Springer, Berlin, Heidelberg, (2007), 117–122.
[31] W. Yin, W. Yang and H. Liu, A neural network scheme for recovering scattering obstacles with limited phaseless far-field data, *Journal of Computational Physics*, **417** (2020), 109594.
[32] F. Zeng, P. Suarez and J. Sun, A decomposition method for an interior inverse scattering problem, *Inverse Problems and Imaging*, **7** (2013), 291–303.
[33] D. Zhang, Y. Wang, Y. Guo and J. Li, Uniqueness in inverse cavity scattering problems with phaseless near-field data, *Inverse Problems*, **36** (2020), 025004.

Received May 2020; 1st revision May 2020; 2nd revision May 2020.

*E-mail address*: yinweishi@foxmail.com
*E-mail address*: givejoywisdom@163.com
*E-mail address*: mengpc@cust.edu.cn
*E-mail address*: qufuheng@163.com